Nuclear Inst. and Methods in Physics Research, A 942 (2019) 162374

Contents lists available at ScienceDirect

Nuclear Inst. and Methods in Physics Research, A

journal homepage: www.elsevier.com/locate/nima

The methodology of characterization of neutron leakage field from PET production cyclotron for experimental purposes

Michal Košťál [a,*], Evžen Losa [a], Martin Schulc [a], Jan Šimon [a], Zdeněk Matěj [b], Michal Antoš [c], Šimon Vadják [c], Martin Cuhra [c], František Cvachovec [d], Filip Mravec [b], Filip Brijar [a], Tomáš Czakoj [a], Vojtěch Rypar [a]

[a] Research Centre Rez, 250 68 Husinec-Rez 130, Czech Republic
[b] Masaryk University, Botanická 15, Brno 612 00, Czech Republic
[c] UJV Rez, 250 68 Husinec-Rez 130, Czech Republic
[d] University of Defence, Kounicova 65, Brno 612 00, Czech Republic

ARTICLE INFO

Keywords:
PET leakage neutron field
Neutron spectrometry
IBA 18/9
Cyclotron
Radiation protection

ABSTRACT

During the production of ^{18}F isotope for radiopharmaceuticals in $^{18}O(p,n)^{18}F$ reactions, the leakage neutrons are mostly considered as a waste product. The utilization of a cyclotron based neutron source might be an interesting application because its average energy is relatively high and emissivity is quite strong. Thus its use might be useful in many fields of neutron based research. This paper aims to define the methodology and its following use for the characterization of the secondary neutron field leaking from ^{18}O enriched H_2O target in IBA Cyclone 18/9. Experimental characterization is based on the employment of independent methods, namely the proton recoil method using a stilbene scintillation detector and neutron activation analysis with selected IRDFF materials. Neutron field characteristics were also tested by calculation in the standard MCNP6 code model and using FENDL-3, TENDL-2017 nuclear data libraries for (p,n) reactions. The calculation models have been found as discrepant in some quantities more or less, thus it is recommended to use experimental characterization as a sole method.

1. Introduction

Although the medical cyclotrons are primarily designed for industrial radioisotope production, they can successfully be used as a research instrument as well. In [1] common IBA Cyclone 18/9 was used for proton induced cross-section measurement. [2] also suggested the use of secondary neutrons in research connected with radiation protection, environmental studies or issues related to the ^{37}Ar detection in nuclear explosions. Another possible use is also a validation of cross-sections, where the neutron field has to be well-defined with low uncertainties. Generally, its knowledge is essential not only for scientific reasons but also for purposes of radiation protection in cyclotron laboratories, because the leaking neutrons can cause exposition of service staff and also activation of cyclotron structural components.

This paper aims to describe the new methodology for characterization of the secondary neutron field quantities, such as the neutron spectrum and the neutron flux. The initial approach of the experimental neutron field characterization was using either Bonner spectrometry [3] or TLD spectrometry [4] or measurement of activation foils [5]. A simple ^{3}He counter with moderation block was used to monitor the neutron flux level [6]. These methods are well usable from a radiation safety point of view [7], however they might be connected with high uncertainties [8–10]. The proton recoil method, namely stilbene scintillation spectrometry seems to be a suitable method for experimental characterization of neutron spectra. The same method is planned to be used as neutron tracker in particle therapy [11]. Because of observed discrepancies between experiments and calculation, the proton recoil method is supported by spectral indexes of various threshold reactions using well-defined, mostly IRDFF, materials. The independent method of spectrum adjustment by STAYSL code, using the measured reaction rates of selected activation foils, was introduced as well.

Measurement of absolute reaction rates allowed the determination of absolute neutron flux. Calculations were performed with a detailed mathematical model of proton induced neutron generation. Thanks to the precise measurement of the produced activity, the validation of the ^{18}F production (and neutron emissivity) comparing the theoretical and experimental $^{18}O(p,n)^{18}F$ reaction rate was possible.

2. Cyclotron arrangement

Neutron field characterization is done in IBA Cyclone 18/9 accelerator (18 MeV for H^-, 9 MeV for D^- particle) which is located in

* Corresponding author.
E-mail address: Michal.Kostal@cvrez.cz (M. Košťál).

https://doi.org/10.1016/j.nima.2019.162374
Received 13 April 2019; Received in revised form 8 July 2019; Accepted 10 July 2019
Available online 15 July 2019

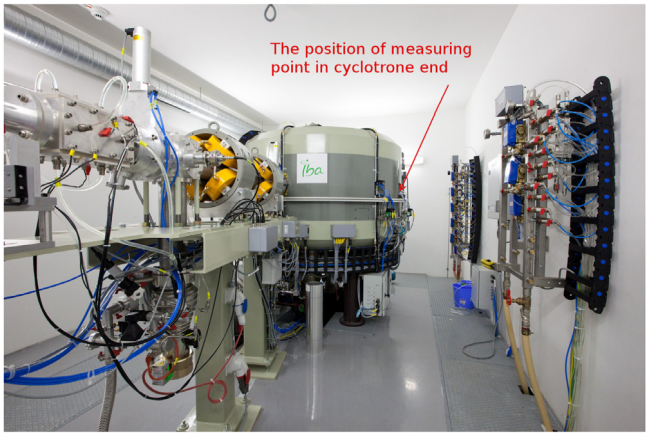

Fig. 1. IBA Cyclotron with marked measuring position.

UJV cyclotron laboratory. The most common radioisotope product of the facility is 2-fluoro-2-deoxy-D-glucose (FDG) labeled by ^{18}F which origins from ^{18}O(p,n)^{18}F reaction. However, the capacity to produce the other positron-emitting radio-nuclides such as ^{11}C, ^{13}N, ^{15}O exists.

Cyclotron device is commissioned inside a 4 m wide and 5.75 m long concrete shielding bunker to avoid irradiation of service staff. The accelerator itself with 2 m diameter is centered to the shorter side and the same distance from the side wall (see Fig. 1).

Measurements were performed during irradiation (by 18 MeV protons) of 2.7 ml ^{18}O enriched water (min. 98%). The water is placed in a niobium pin (see Fig. 2) which is sealed by a Havar foil, while accelerator window is sealed by a Ti foil. The current generated by the proton beam on the target was ~75 μA in case of the activation experiment, while at stilbene experiments it was 0.92 μA.

Neutron spectra were measured at 80 cm from the end of the cyclotron in the direct position in its axis. The activation detectors were irradiated in the same axis and in the positions on cyclotron end and 7.5 cm and 80 cm from the end of the cyclotron. For the study of angular distribution some foils were placed also 8.5 cm below the target axis.

3. Experimental and calculation methods

The set of neutron spectra in the 0.9 MeV to 14.5 MeV energy range was measured via the proton-recoil method using a Stilbene scintillator (10 × 10 mm) with neutron and gamma pulse shape discrimination. The characteristic of signal evaluation is plotted in Fig. 3.

The spectral indexes were derived from the reaction rates. The experimental reaction rates were derived from the gamma activities of irradiated samples. The induced dosimeter activity after irradiation in the studied neutron field was determined using a well-defined HPGe detector with verified geometry and efficiency. These quantities are described in detail in [13]. The calculations were realized using the MCNP6 code [14], with various nuclear data libraries.

3.1. Stilbene measurement

The upgraded two-parameter spectrometric system NGA-01 [15–17] is fully digitized and is now able to process up to 500 000 impulse responses per second. In the described case, the tapered active voltage divider was used for the photomultiplier tube [18]. This type of divider has better output linearity than previously used passive resistance, where the problem with non-linearity could exist even from relatively low rate of about 10^4 impulses per second. Solving the non-linearity problem with active voltage divider based on MOSFETs also solves the problem of non-linearity depending on the amplitude of the signal.

A large dynamic range of input signal is required for measurement. Therefore, the input analog signal from the photomultiplier is divided into two branches with different ratio of amplification (1:8). The signal is then digitized by separate analog to digital converters with 12-bit resolution. A high-pass filter is used for better resolution. The difference in amplification increases the signal-to-noise ratio. Analog-to-digital converters operating at a sampling frequency of 500 MHz are used, and digital signal processing is implemented in the field-programmable gate array (FPGA). Therefore, it can process all the data flow from both analog to digital converters with negligible dead time in the

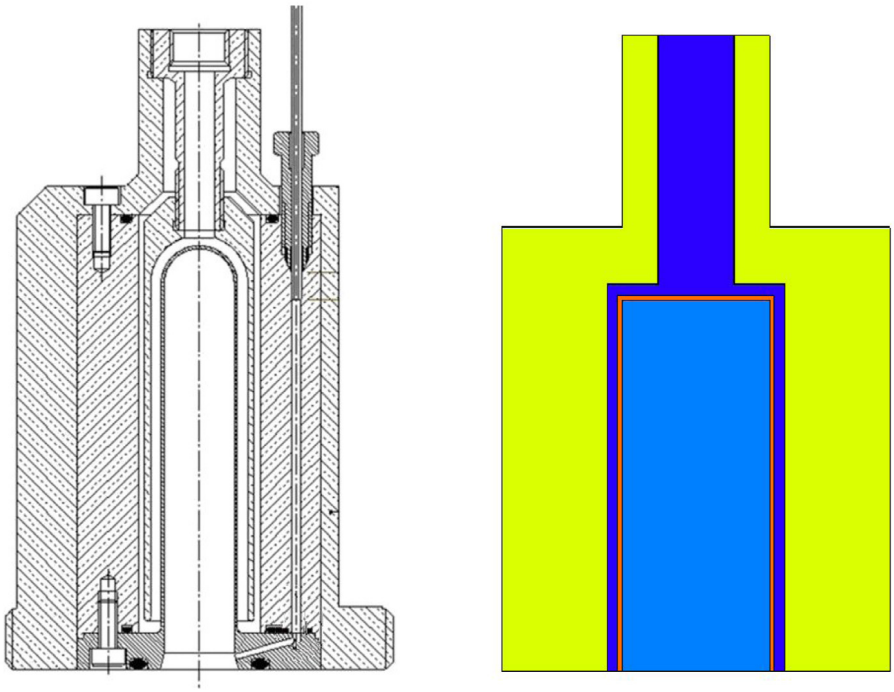

Fig. 2. Target with ^{18}O enriched H_2O target full (left) [12] and simplified used in simulations (right).

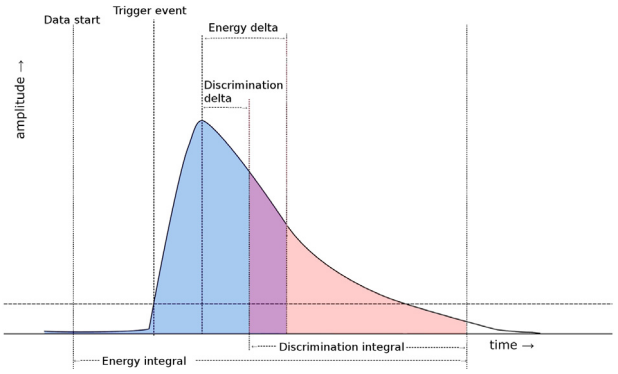

Fig. 3. Characteristics of evaluation of signal. Energy integral is taken from data start to peak with energy delta, discrimination integral from the peak with discrimination delta to the data end.

digital part. Problems at high frequencies ($> 10^5$ pulses per second) are superpositions on signals that can affect the resulting values. These pulses are largely filtered [19].

Pulse Shape Discrimination (PSD) unit is used to distinguish the type of the detected particle by analyzing the pulse shape (discrimination integral), whereas particle energy is evaluated from the integral of the whole response (energy integral). The PSD value is computed inside the FPGA by an integration method which uses the comparison of the area delimited by part of a trailing edge of the measured response with the area delimited by the whole response. See Fig. 3 for the principle of the PSD used; the method is more in detail described for example in [19]. Acquired recoiled proton spectra (or electron spectra in case of gamma field measurement) are then subjected to deconvolution by the Maximum Likelihood Estimation [20].

3.2. Reaction rates measurement

The experimental reaction rates were derived from the dosimeter (activation detector) activity (see Eqs. (1), (2)). This monitor activity was determined by employing gamma spectrometry with HPGe detector with well defined efficiency curve [13]. In the case of coincidences, the correction factor was employed, as mentioned in [21]. Various types of dosimeters were used, pure natural Ni, Fe, Al, Cu, and Ti. The evaluated monitoring reactions were: ^{58}Ni(n,p), ^{60}Ni(n,p), ^{58}Ni(n,x)^{57}Co, ^{54}Fe(n,p), ^{48}Ti(n,p), ^{27}Al(n,α), ^{63}Cu(n,α). The detailed summary of used activation dosimeters is listed in Table 1. The dosimeters were measured in the end cap geometry.

$$A_{End.} = NPA\left(\mathrm{T}_{Meas.}\right) \times \frac{\lambda}{\varepsilon \times \eta \times N} \times \frac{1}{\left(1 - e^{-\lambda.\mathrm{T}_{Meas.}}\right)} \times \frac{1}{e^{-\lambda.\Delta\mathrm{T}}} \times k_{TSCF} \quad (1)$$

$$q = \frac{A_{End.}}{1 - e^{-\lambda.\mathrm{T}_{Irr.}}} \quad (2)$$

where:

q; is the reaction rate of activation during irradiation batch

λ; is the decay constant of the radioisotope considered;

$\mathrm{T}_{Meas.}$; is a time of measurement by the HPGe;

ΔT; is the time between the end of irradiation and the start of the HPGe measurement;

$NPA(\mathrm{T}_m)$; is the Net Peak Area (the measured number of counts);

ε; is the gamma branching ratio;

η; is the detector efficiency (it is being determined via MCNP6 calculation);

N; is the number of target isotope nuclei;

k_{TSCF} is coincidence summing correction factor

$\mathrm{T}_{\mathrm{Irr.}}$; is the end of the irradiation period

Table 1
Used activation detectors.

Foil	Dimensions	Reaction	Peak [keV]	Efficiency	CSCF
Fe	1 × 1 × 0.3 cm	^{54}Fe(n,p)	834.8	3.504 × 10^{-2}	1.000
		^{54}Fe(n, α)	320.1	7.466 × 10^{-2}	1.000
Ni	1.6 × 1.6 × 0.1 cm	^{58}Ni(n,p)	810.8	4.586 × 10^{-2}	0.933
		^{60}Ni(n,p)	1173.0	3.428 × 10^{-2}	0.824
			1332.5	3.086 × 10^{-2}	0.818
		^{58}Ni(n,x)^{57}Co	122.1	1.489 × 10^{-1}	1.000
Al	D=1.27, th. 0.3 cm	^{27}Al(n, α)	1368.6	2.910 × 10^{-2}	0.862
Ti	0.9 × 0.9 × 0.1 cm	^{48}Ti(n,p)	983.5	4.054 × 10^{-2}	0.648
			1037.5	3.885 × 10^{-2}	0.641
			1312.1	3.210 × 10^{-2}	0.629
		^{46}Ti(n,p)	889.3	4.397 × 10^{-2}	0.820
		^{47}Ti(n,p)	159.4	1.703 × 10^{-1}	1.000
Cu	1 x 1 x 0.4 cm	^{63}Cu(n, α)	1173.0	3.001 × 10^{-2}	0.841
			1332.5	2.717 × 10^{-2}	0.837

3.3. STAYSL adjustment of neutron spectra

In addition to measurements with the stilbene scintillator, the neutron spectrum was adjusted with STAYSL code using measured reaction rates. STAYSL PNNL is a suite of programs that includes STAYSL itself and various supporting utilities [22] containing a variant of code STAY'SL [23] developed by Dr. Perey at Oak Ridge National Laboratory. Given a set of neutron activation rates measured in a nuclear fission reactor or at an accelerator based neutron source, STAYSL PNNL uses least-square fitting methods to solve the dosimetry neutron spectral adjustment problem and thus determines the most likely neutron flux spectrum [22]. This process is referred to as neutron spectral adjustment [24,25]. Neutron spectrum adjustment is carried out in order to find a spectrum which, for a specified dosimetry cross section, will give the most likely fit to the set of measured activities.

In order to perform the spectral adjustment, the following quantities must be calculated by individual part of STAYSL PNNL suite: corrected activation rates (calculated by SigPhi Calculator), the neutron self-shielding correction factors (SHIELD code), cross-sections and covariance data libraries (NJOY99/NJpp), and initial neutron flux spectrum estimation (preferably from code such as MCNP). For further details and mathematical description of the process see [22,23].

3.4. Calculation methods

The calculations were performed using the MCNP6 Monte Carlo code in proton/neutron transport mode and except proton data libraries the default model settings were tested for (p,n) reactions with 18 MeV protons. In the MCNP6 model testing, default settings containing the Cascade–Exciton Model (CEM) model is used for nuclear interactions of accelerated protons. The CEM model, originally proposed in Dubna, incorporates all three stages of nuclear reactions: intranuclear cascade, pre-equilibrium, and equilibrium (or compound nucleus) [26,27], where mostly pre-equilibrium and equilibrium stages are applicable to our problem. The neutron emission spectrum, in this case, is close to the evaporation model [28,29] used in [5]. However the one obtained from the CEM model should perform better in terms of the neutron angular distribution. Better results are attributed to the anisotropy treatment of released secondary neutrons [26]. After the evaporation, the MCNP code models are accounting de-excitation phase by gamma emission [14].

For comparison, the employment of ^{18}O(p,n)^{18}F libraries from TENDL-2017 [30] and FENDL-3 [31] were also tested. ENDF/B-VII.1 nuclear data library was used for simulation of neutron interactions in structural materials and for ^{58}Ni(n,x)^{57}Co reaction. All other monitors' cross sections were described using IRDFF v.1.05 [32,33] (see Fig. 8).

It is worth noting that the structural components have special importance in the formation of the secondary neutron field. It is evident

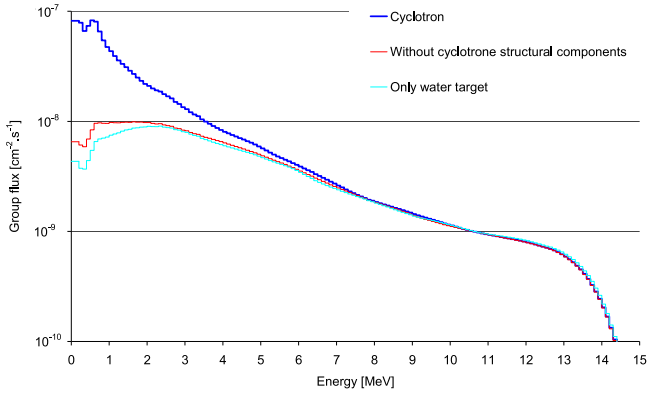

Fig. 4. Comparison of calculated neutron spectra 80 cm from cyclotron end showing the effect of structural components on the neutron field.

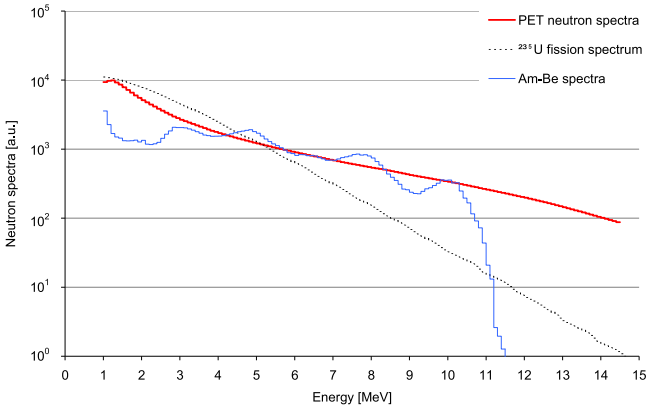

Fig. 5. Comparison of various sources' neutron spectrum.

that the low part of the neutron spectrum is generated by the room effect (see Fig. 4). The uncertainties in the calculated reaction rates are below 2%. Hence the calculation uncertainties in the spectral indexes and attenuation factors are less than 3%. The uncertainties in the neutron fluence rate are about 2% in lower regions and 5 - 9% in upper regions.

4. Results

4.1. Differential neutron spectra

The neutron spectrum in position 80 cm from ^{18}O enriched H_2O target was measured using 10×10 mm stilbene detector. It is formed by the evaporation process; thus its shape is different from other common sources (see Fig. 5).

The resulted spectrum of MCNP6 models compared with calculations using various proton induced data libraries are presented in Fig. 6 and listed in Table 2. The listed experimental uncertainties cover statistical uncertainty, uncertainty in energy and efficiency calibration and uncertainty in the evaluation method. It is obvious that from the presented results, the most reasonable agreement with experiment is in the case of MCNP6 models. However, even in this case, significant discrepancies can be found. The C/E−1 comparison is presented in Fig. 7. From this graph, it is clear that the discrepancy in the 2–6 MeV interval is 2–3 times higher than the related uncertainty and in the region around 10 MeV, even higher than 5 times the respective uncertainty.

The calculations realized with TENDL-2017, and FENDL-3 do not differ significantly in the region below 6 MeV. In the upper region, they begin to diverge from the others. In a region above 10 MeV, the discrepancies are obvious.

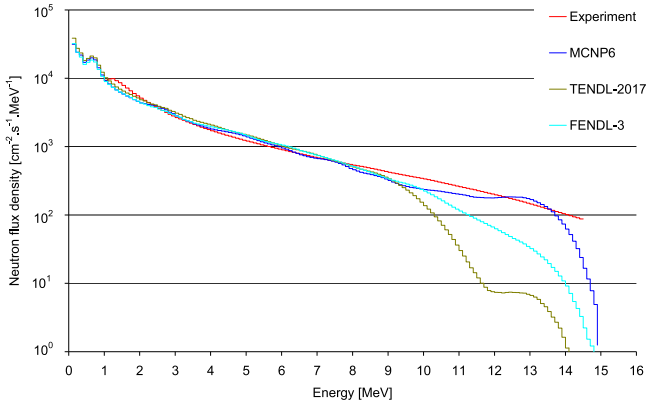

Fig. 6. Calculated and stilbene scintillator measured neutron spectrum 80 cm from cyclotron end.

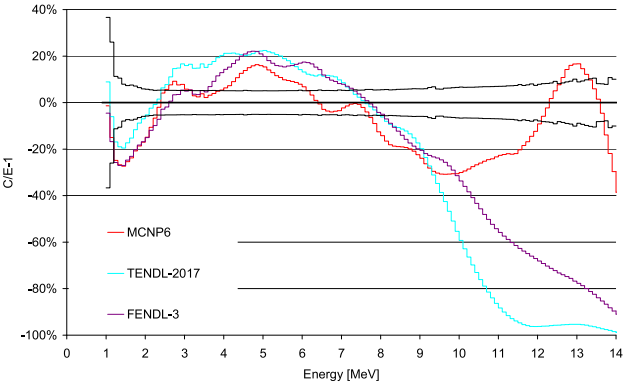

Fig. 7. C/E−1 of calculated and measured neutron spectrum 80 cm from cyclotron end.

4.2. Spectral indexes

Comparison of measurements with the stilbene scintillator with calculation shows significant discrepancies, especially in higher energy regions. To confirm that the reported discrepancies are not caused by measurements with the stilbene scintillator (resolution problems, efficiency problems), they were supplemented by evaluation of the spectral indexes (see Eq. (4)) which were derived from reaction rates of IRDFF materials [32,33]. The spectral indices are an important tool used for characterization of the shape of a neutron spectrum [34]. They are defined as a ratio of the observed reaction rate to the reference rate. Reaction rates ratio is independent on the absolute neutron flux.

$$RR_A = \int_E \sigma_A(E) \times \varphi(E)\, dE = n \times \int_E \sigma_A(E) \times \psi(E)\, dE \tag{3}$$

$$\left(\frac{RR_A}{RR_B}\right) = \frac{\int_E \sigma_A(E) \times \varphi(E)\, dE}{\int_E \sigma_B(E) \times \varphi(E)\, dE} = \frac{\int_0^\infty \sigma_A(E) \times \psi(E)\, dE}{\int_0^\infty \sigma_B(E) \times \psi(E)\, dE} \tag{4}$$

$\sigma_A(E)$	Cross section of reaction A
$\varphi(E)$	Neutron flux density
n	Neutron flux
$\psi(E)$	Neutron spectrum ($\int_0^\infty \psi(E)\, dE = 1$)

Table 2
Measured group neutron flux, 80 cm from cyclotron end, normalized per 1 proton emitted from the accelerator.

E_{up}	dΦ [cm^{-2} s^{-1}]	Rel. unc. [%]	E_{up}	dΦ [cm^{-2} s^{-1}]	Rel. unc. [%]	E_{up}	dΦ[cm^{-2} s^{-1}]	Rel. unc. [%]	E_{up}	dΦ [cm^{-2} s^{-1}]	Rel. unc. [%]
1.0	1.20×10^{-9}	11.7	4.5	2.56×10^{-10}	4.1	8.0	9.57×10^{-11}	4.6	11.5	4.06×10^{-11}	6.9
1.1	1.63×10^{-9}	7.4	4.6	2.48×10^{-10}	4.2	8.1	9.34×10^{-11}	4.7	11.6	3.95×10^{-11}	7.3
1.2	1.70×10^{-9}	11.0	4.7	2.39×10^{-10}	4.1	8.2	9.16×10^{-11}	4.7	11.7	3.84×10^{-11}	7.0
1.3	1.72×10^{-9}	5.5	4.8	2.32×10^{-10}	4.0	8.3	8.97×10^{-11}	4.6	11.8	3.73×10^{-11}	7.4
1.4	1.60×10^{-9}	9.3	4.9	2.24×10^{-10}	4.0	8.4	8.77×10^{-11}	4.7	11.9	3.63×10^{-11}	7.7
1.5	1.50×10^{-9}	7.2	5.0	2.17×10^{-10}	4.0	8.5	8.57×10^{-11}	4.8	12.0	3.53×10^{-11}	7.3
1.6	1.37×10^{-9}	6.1	5.1	2.10×10^{-10}	4.1	8.6	8.37×10^{-11}	4.9	12.1	3.43×10^{-11}	7.9
1.7	1.25×10^{-9}	5.6	5.2	2.03×10^{-10}	4.1	8.7	8.16×10^{-11}	5.0	12.2	3.33×10^{-11}	8.3
1.8	1.14×10^{-9}	5.4	5.3	1.97×10^{-10}	4.1	8.8	7.95×10^{-11}	4.9	12.3	3.23×10^{-11}	8.6
1.9	1.04×10^{-9}	4.9	5.4	1.91×10^{-10}	4.1	8.9	7.75×10^{-11}	5.0	12.4	3.14×10^{-11}	8.9
2.0	9.65×10^{-10}	4.5	5.5	1.85×10^{-10}	4.1	9.0	7.55×10^{-11}	5.0	12.5	3.05×10^{-11}	9.6
2.1	8.92×10^{-10}	4.6	5.6	1.80×10^{-10}	4.1	9.1	7.35×10^{-11}	5.0	12.6	2.96×10^{-11}	8.9
2.2	8.30×10^{-10}	4.5	5.7	1.74×10^{-10}	4.1	9.2	7.19×10^{-11}	5.0	12.7	2.87×10^{-11}	9.6
2.3	7.70×10^{-10}	4.4	5.8	1.70×10^{-10}	4.1	9.3	7.03×10^{-11}	5.6	12.8	2.78×10^{-11}	10.4
2.4	7.19×10^{-10}	4.4	5.9	1.65×10^{-10}	4.1	9.4	6.86×10^{-11}	5.8	12.9	2.69×10^{-11}	11.2
2.5	6.70×10^{-10}	4.5	6.0	1.60×10^{-10}	4.3	9.5	6.70×10^{-11}	5.2	13.0	2.60×10^{-11}	12.4
2.6	6.28×10^{-10}	4.3	6.1	1.56×10^{-10}	4.2	9.6	6.55×10^{-11}	5.3	13.1	2.51×10^{-11}	11.9
2.7	5.88×10^{-10}	4.4	6.2	1.52×10^{-10}	4.1	9.7	6.40×10^{-11}	5.3	13.2	2.42×10^{-11}	13.1
2.8	5.52×10^{-10}	4.4	6.3	1.47×10^{-10}	4.2	9.8	6.26×10^{-11}	5.7	13.3	2.34×10^{-11}	13.1
2.9	5.17×10^{-10}	4.3	6.4	1.44×10^{-10}	4.2	9.9	6.13×10^{-11}	5.6	13.4	2.26×10^{-11}	14.5
3.0	4.90×10^{-10}	4.3	6.5	1.40×10^{-10}	4.5	10.0	6.00×10^{-11}	5.7	13.5	2.18×10^{-11}	16.2
3.1	4.63×10^{-10}	4.3	6.6	1.36×10^{-10}	4.3	10.1	5.86×10^{-11}	5.8	13.6	2.11×10^{-11}	14.1
3.2	4.42×10^{-10}	4.3	6.7	1.33×10^{-10}	4.3	10.2	5.72×10^{-11}	5.8	13.7	2.03×10^{-11}	15.8
3.3	4.22×10^{-10}	4.2	6.8	1.29×10^{-10}	4.3	10.3	5.58×10^{-11}	5.7	13.8	1.96×10^{-11}	15.9
3.4	4.03×10^{-10}	4.2	6.9	1.26×10^{-10}	4.3	10.4	5.44×10^{-11}	5.8	13.9	1.89×10^{-11}	18.5
3.5	3.84×10^{-10}	4.2	7.0	1.22×10^{-10}	4.5	10.5	5.30×10^{-11}	5.9	14.0	1.83×10^{-11}	18.6
3.6	3.67×10^{-10}	4.2	7.1	1.19×10^{-10}	4.2	10.6	5.15×10^{-11}	5.9	14.1	1.76×10^{-11}	19.0
3.7	3.51×10^{-10}	4.2	7.2	1.16×10^{-10}	4.2	10.7	5.01×10^{-11}	6.0	14.2	1.70×10^{-11}	19.8
3.8	3.36×10^{-10}	4.3	7.3	1.13×10^{-10}	4.3	10.8	4.88×10^{-11}	6.2	14.3	1.64×10^{-11}	20.8
3.9	3.21×10^{-10}	4.2	7.4	1.10×10^{-10}	4.8	10.9	4.76×10^{-11}	6.1	14.4	1.58×10^{-11}	22.4
4.0	3.09×10^{-10}	4.2	7.5	1.08×10^{-10}	4.5	11.0	4.63×10^{-11}	6.0	14.5	1.52×10^{-11}	24.0
4.1	2.97×10^{-10}	4.1	7.6	1.05×10^{-10}	4.4	11.1	4.51×10^{-11}	6.3	14.6	1.49×10^{-11}	24.0
4.2	2.86×10^{-10}	4.1	7.7	1.03×10^{-10}	4.7	11.2	4.39×10^{-11}	6.3	14.7	1.45×10^{-11}	24.0
4.3	2.76×10^{-10}	4.1	7.8	1.00×10^{-10}	4.9	11.3	4.28×10^{-11}	6.3			
4.4	2.66×10^{-10}	4.1	7.9	9.79×10^{-11}	4.6	11.4	4.17×10^{-11}	6.8			

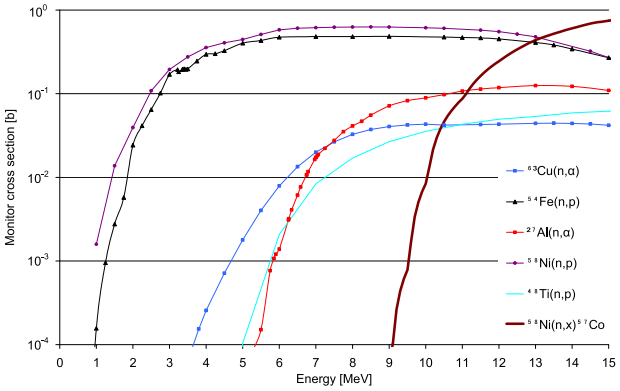

Fig. 8. Cross sections used for spectrum index determination.

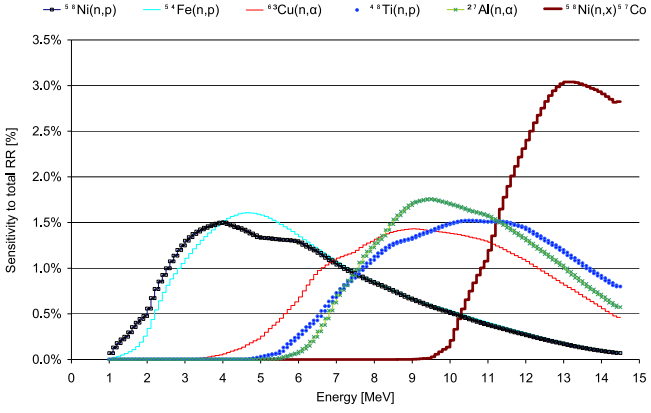

Fig. 9. Sensitivity of used reaction rates for various energy in measured spectra.

The energy dependence of cross sections used in spectrum index comparison is plotted in Fig. 8, the sensitivities in the stilbene scintillator measured spectrum are plotted in Fig. 9. The summary of spectrum indexes is in Table 3.

It is obvious that there are significant discrepancies between experiment and calculation. The spectral ratio of ^{54}Fe(n,p)/^{27}Al(n, α) supports the result that both TENDL-2017 and FENDL-3 are strongly underestimating experiment in the region above 7 MeV because the calculated ratio is about 60%–150% higher than the experiment. This higher rate of overestimation reflects the problems in describing the high-energy tail of the neutron spectrum. In the case of the neutron spectrum calculated by MCNP6 models (CEM), the ratio is higher by 18%. The obtained result is seemingly consistent when compared with TENDL-2017 and FENDL calculations. But a closer look at the neutron spectrum measurement by stilbene scintillator (Figs. 6 and 7) would suggest that this agreement is a consequence of compensating effects caused by the neutron spectrum shape as a product of CEM model. The issue of the correct description of the neutron spectrum high energy tail is well-answered in ^{58}Ni(n,p)/^{58}Ni(n,x)^{57}Ni spectral index where MCNP6 model differs by 3%, while FENDL-3 and TENDL-2017 results are 4 or 30 times higher than an experiment. This result points to large differences in the region above 9 MeV because the threshold energy of ^{58}Ni(n,x)^{57}Ni is 9 MeV and maximum sensitivity in the measured spectrum lies in the energy of 12.7 MeV, where the differences between spectra are the most dramatic.

The sensitivities in stilbene measured energy spectrum are shown in Fig. 9.

Using deconvolution codes, the neutron spectrum can be derived from a set of reaction rates. The neutron spectrum for the position

Table 3
Spectral indexes in position 7.5 cm from cyclotron end.

	^{54}Fe(n,p)/^{27}Al(n,α)	^{54}Fe(n,p)/^{48}Ti(n,p)	^{54}Fe(n,p)/^{58}Ni(n,p)	^{58}Ni(n,p)/^{58}Ni(n,x)^{57}Co
MCNP6	20.83	50.39	0.77	19.21
FENDL-3	30.26	76.96	0.77	73.64
TENDL-2017	42.92	110.13	0.76	487.54
Experiment	17.05	41.31	0.68	17.42
Rel. unc.	8.6%	8.3%	7.8%	4.2%

Table 4
Measured reaction rates in various positions from target normalized per 1 proton.

	Cyclotron end		80 cm distance		8.5 cm below target	
	Mean	Rel. unc.	Mean	Rel. unc.	Mean	Rel. unc.
^{58}Ni(n,p)	–	–	7.05×10^{-33}	4.5%	–	–
^{54}Fe(n,p)	1.16×10^{-31}	3.9%	5.16×10^{-33}	4.6%	4.65×10^{-31}	3.7%
^{54}Fe(n,α)	4.42×10^{-33}	12.4%	2.38×10^{-34}	12.0%	1.68×10^{-32}	8.6%
^{27}Al(n,α)	7.15×10^{-33}	3.6%	3.36×10^{-34}	4.5%	–	–
^{60}Ni(n,p)	–	–	5.44×10^{-34}	12.5%	–	–
^{58}Co(n,x)^{57}Co	–	–	4.40×10^{-34}	4.9%	–	–
^{63}Cu(n,α)	2.26×10^{-33}	4.1%	–	–	9.87×10^{-33}	4.9%

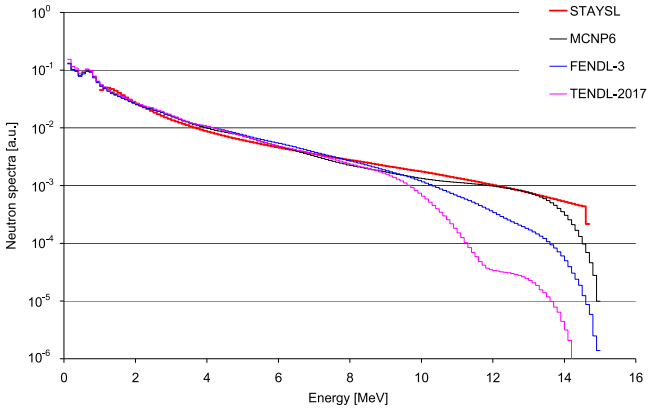

Fig. 10. Comparison of measurement, calculations and STAYSL adjustment of neutron spectrum 7.5 cm from cyclotron end.

7.5 cm from the cyclotron end was derived by STAYSL code from following reactions: ^{58}Ni(n,p), ^{27}Al(n, α), ^{54}Fe(n,p), ^{54}Fe(n, α), ^{48}Ti(n,p), ^{46}Ti(n,p), ^{47}Ti(n,p), ^{63}Cu(n, α), ^{60}Ni(n,p). The result compared with the stilbene scintillator measurement and MCNP6 calculations are plotted in Fig. 10. It can be said that the STAYSL results for the neutron spectrum are closer to stilbene measurement than to calculations using proton libraries and models.

4.3. Distribution of neutron fluxes

The reaction rate is a function of the reaction cross section and the actual neutron spectrum (see Eq. (3)). Assuming known cross section, this can be used for the determination of neutron flux. It means that the reaction rates listed in Table 4 can be used to characterize the integral neutron flux at different positions from the ^{18}O target. The C/E−1 comparison for a position in cyclotron end and in distance 80 cm in its vertical axis from the target is listed in Tables 5 and 6.

The agreement is satisfactory in some separate cases but generally is not very good. It means that the proton libraries and mathematical model (TENDL-2017, FENDL-3, MCNP6) are not satisfactory for the correct description of the neutron field. The discrepancy rate seems to be comparable in both distances from the target. This fact is reflected in similar calculated and measured attenuation of reaction rates between positions at the end of the cyclotron and 80 cm behind it (see Table 7). As the results of the attenuation calculation are in good agreement with the experimentally determined attenuation, it can be stated that the mathematical description of neutron flux attenuation in forwarding transport is satisfactory.

Table 5
C/E-1 of measured reaction rates in end of the cyclotron.

	MCNP6	FENDL-3	TENDL-2017
^{54}Fe(n,p)	21.7%	25.7%	−1.9%
^{54}Fe(n, α)	14.9%	−10.4%	−43.8%
^{27}Al(n, α)	−6.5%	−34.3%	−63.2%
^{63}Cu(n, α)	35.5%	6.2%	−33.6%

Table 6
C/E-1 of measured reaction rates 80 cm from cyclotron end.

	MCNP6	FENDL-3	TENDL-2017
^{58}Ni(n,p)	13.4%	23.1%	−2.8%
^{54}Fe(n,p)	19.8%	29.4%	1.4%
^{54}Fe(n,α)	−5.0%	−20.6%	−49.3%
^{27}Al(n,α)	−13.2%	−34.1%	−62.2%
^{60}Ni(n,p)	−7.3%	−18.9%	−47.0%
^{58}Ni(n,x)^{57}Co	−2.5%	−73.2%	−96.3%

Table 7
Reaction rates attenuation factor between positions in end of the accelerator and in 80 cm distance in the vertical axis.

Attenuation	MCNP6	FENDL-3	TENDL-2017	Experiment	Exp. unc.
^{54}Fe(n,p)	22.7	21.7	21.7	22.4	5.0%
^{27}Al(n,α)	22.9	21.2	20.7	21.3	5.6%

4.4. Angular distribution

The axially located position is the most important one for the utilization of secondary neutrons due to the dependence of flux and distance from the source. However, the angular distribution (see Fig. 11) is also important, because it affects the neutron field around the target. This neutron field can contribute to the positions close to the exit window and is also responsible for the activation of accelerator structural components. Due to the high flux and small space in the exit window, the angular profile determination is based on the reaction rates. The ratio of reaction rate below target to reaction rate in the exit window is about 4 in case of ^{54}Fe(n,p) and 4.4 in case of ^{63}Cu(n,α). Assuming the point character of the neutron source and taking into account about twice longer path of ^{18}O(p,n) neutrons into the target in the vertical axis, the result implies a nearly isotropic distribution of neutrons. The assumption of similar neutron spectrum shape in various angles is confirmed by similar spectral indexes (see Table 9). This trend is not followed by calculation. The calculation models seem to be incorrect, namely highly under-predicting in higher energies, because the reaction rates of higher energy threshold reactions are significantly under-predicting the experimental value (see Table 8).

Table 8
C/E-1 of measured reaction rates 8.5 cm below the target axis.

	MCNP6	FENDL-3	TENDL-2017
^{54}Fe(n,p)	4.5%	29.1%	−2.7%
^{54}Fe(n,α)	−67.8%	−29.0%	−59.6%
^{63}Cu(n,α)	−68.2%	−31.6%	−61.0%

Table 9
Spectral index ^{54}Fe(n,p)/^{63}Cu(n,α) in various angles regarding to proton beam.

	MCNP6	FENDL-3	TENDL-2017	Experiment	Exp. unc.
Below target	155.0	88.9	117.6	47.1	6.1%
In axis	46.3	60.6	76.7	51.1	5.6%

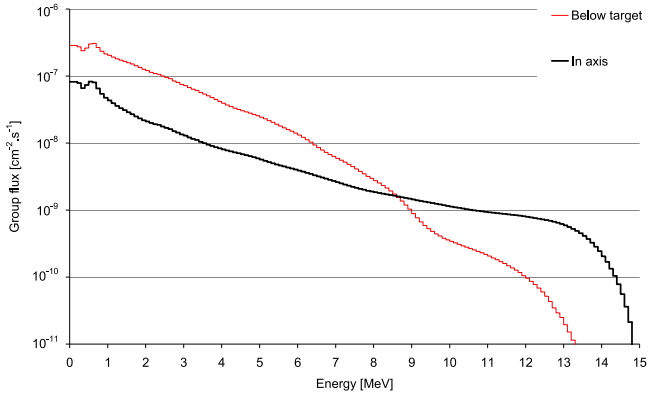

Fig. 11. Calculated neutron spectrum below target and in the exit window.

4.5. Validation of source neutron emission

The neutrons are emitted from ^{18}O(p,n)^{18}F reaction. It means that neglecting neutrons from (p,n) reactions in Havar and Ti structural foils; the neutron emission is identical with ^{18}F production rate. Thanks to this fact, the comparison between real and theoretical production was compared to 3.5 min after irradiation. The activity of produced ^{18}F was measured in certified geometry, within 5% uncertainty. The TENDL-2017 [30] cross section of ^{18}O(n,p)^{18}F reaction was used in this evaluation because of good agreement with experimental cross sections [35]. The production rate of ^{18}F seems to be correct, as it was many times validated.

From the radiation safety point of view, ^{18}F enriched H_2O is transferred from the cyclotron cell by piping. It was determined that in the used standard target, 6.9% of the total activity induced in the target during irradiation by protons remains in pipes. Taking into account this correction, the C/E−1 of ^{18}F activity was determined to be 0.03. Knowing that purity of ^{18}O in the enriched water is about 98%, it can be concluded that the agreement is very good. These results are interesting because [36] report that in the case of applying the same TENDL-2017 libraries the GEANT code under-predicts is by a factor of 0.53, while FLUKA over-predicts by a factor of 1.66. The summary of the experimental results is listed in Table 10.

5. Validation of selected cross sections in ^{18}O(p,n)^{18}F field

The developed methodology of characterization of ^{18}F production cyclotron was applied to the set of measured dosimeters in position 80 cm from the cyclotron end (see Table 11). The dosimeters sensitive in various energy regions were used. The reaction rates obtained with developed characterization are in satisfactory agreement with experiment. The related uncertainties of experimental reaction rates are listed in Table 4, the uncertainties of reaction rates calculated using characterized spectra are ~6% – 8%. The main source of uncertainty is uncertainty in characterized neutron spectra.

Table 10
Validation of ^{18}F production.

Validated parameter	Mean value
A (measured) [Bq]	189.3
Correction to decay during transport	1.022
Correction to piping residual activity	1.069
A (produced) [Bq]	206.9 ± 5.2
T [s]	5940
Current [μA]	51.79
RR [^{18}F/1p]	1.42×10^{-3}
A (TENDL) [Bq]	213.2 ± 0.4
C/E-1	3.10%

Table 11
Validation of selected IRDFF cross sections in the experimentally characterized field (EVAL/E-1).

Reaction	EVAL/E-1
^{27}Al(n,α)	−4.9%
^{54}Fe(n,p)	12.9%
^{54}Fe(n,α)	0.1%
^{58}Ni(n,p)	7.6%
^{60}Ni(n,p)	−2.8%
^{58}Ni(n,x)^{57}Co	−7.1%

6. Conclusions

The methodology of characterization of leakage neutron field of the ^{18}F production cyclotron was presented and applied for IBA Cyclone 18/9 cyclotron with XL cylindrical target. The tested mathematical models and proton libraries show significant discrepancies; thus they are not suitable for a precise description of the secondary neutron field to be used as a scientific instrument.

The TENDL-2017 and FENDL-3 libraries differ significantly in the shape of the spectrum in the high-energy tail, whereas MCNP6 default model is incorrect in angular distribution. Regarding the calculations of the ^{18}F production yields, the MCNP6 seems to be a useful tool in combination with TENDL-2017 proton library, because the calculation to experiment discrepancy is about 3% and is comparable with respective uncertainties.

The neutron spectrum can be effectively characterized using stilbene scintillation spectrometry, the flux with neutron activation analysis. When the dosimeters are properly selected, the ratio of reaction rates can be effectively used for adjustment of the spectrum shape. Very useful seems to be the ^{58}Ni(n,p) / ^{58}Ni(n,x)^{57}Co spectral ratio because as it is evaluated from one dosimeter and many of the uncertainties are suppressed. A leakage neutron field is an interesting option for irradiation experiments due to quite high flux, but also for the validation of high energy threshold reactions due to relatively high average energy. This type of experiments generally has a very high scientific potential, as radioisotopes production and research can take place simultaneously. The NGA-01 spectrometer has proven to be suitable for measurements in fields formed by evaporation neutrons.

Acknowledgments

Presented results were obtained with the use of the infrastructure Reactors LVR-15 and LR-0, which is financially supported by the Ministry of Education, Youth and Sports Czech Republic - project LM2015074 and - project LQ1603 Research for SUSEN. This work has been realized within the SUSEN Project (established in the framework of the European Regional Development Fund (ERDF) in project CZ.1.05/2.1.00/03.0108 and of the European Structural Funds and Investment Funds (ESIF), Czech Republic in the project CZ.02.1.01/0.0/0.0/15_008/0000293), which is financially supported by the Ministry of Education, Youth and Sports, Czech Republic - project LM2015093 Infrastructure SUSEN and with the support of the mathematical and physical research project of [37].

References

[1] S.T. Carzaniga S. Braccini, Cross-section measurement of ^{44m}Sc,^{47}Sc,^{48}Sc and^{47}Ca for an optimized^{47}Sc production with an 18 MeV medical PET cyclotron, Appl. Radiat. Isot. 143 (2019) 18–23.

[2] S. Braccini, Compact medical cyclotrons and their use for radioisotope production and multi-disciplinary research, in: Proceedings of the Cyclotrons, 2016, pp. 229–234, http://accelconf.web.cern.ch/AccelConf/cyclotrons2016/papers/tud01.pdf.

[3] Héctor René Vega-Carrillo, Neutron energy spectra inside a PET cyclotron vault room, Nucl. Instrum. Methods Phys. Res. A 463 (1–2) (2001) 375–386.

[4] A.M. Guimarães, M.A.S. Lacerda, J.A.L. Santos, P.G.M. Malett, S.L.M. Rodrigues, R.S. Andrade, E.C. Vilela, T.A. da Silva, Use of a TLD-based multisphere spectrometry system to measure the neutron spectra around a not-self-shielded PET cyclotron: Preliminary results, Appl. Radiat. Isot. 71 (2012) 92–95.

[5] D. Alloni, M. Prata, Characterisation of the secondary neutron field generated by a compact PET cyclotron with MCNP6 and experimental measurements, Appl. Radiat. Isot. 128 (2017) 204–209.

[6] Yuan-Hao Liu, Rong-Jiun Sheu, Jui-Chang Chang, Kuo-Wei Yin, Shiang-Huei Jiang, A study on the [18F]FDG production efficiency of the MINItrace™ cyclotron in Shin Kong Memorial Hospital, Nucl. Instrum. Methods Phys. Res. A 562 (2) (2006) 1064–1067.

[7] J.C. McDonald, B.R.L. Siebert, W.G. Alberts, Neutron spectrometry for radiation protection purposes, Nucl. Instrum. Methods Phys. Res. A 476 (2002) 347–352.

[8] F.D. Brooks, H. Klein, Neutron spectrometry—historical review and present status, Nucl. Instrum. Methods Phys. Res. A 476 (2002) 1–11.

[9] D.J. Thomas, A.V. Alevra, Bonner sphere spectrometers—a critical review, Nucl. Instrum. Methods Phys. Res. A 476 (2002) 12–20.

[10] S.P. Tripathy, C. Sunil, M. Nandy, P.K. Sarkara, D.N. Sharma, B. Mukherjeed, Activation foils unfolding for neutron spectrometry: Comparison of different deconvolution methods, Nucl. Instrum. Methods Phys. Res. A 583 (2007) 421–425.

[11] M. Marafini, V. Patera, D. Pinci, A. Sarti, A. Sciubba, E. Spiriti, MONDO: A neutron tracker for particle therapy secondary emission fluxes measurements, Nucl. Instrum. Methods Phys. Res. A 824 (2016) 210–211.

[12] J. Courtyn, F. Devillet, Jean-Michel Geets, et al., Performance of IBA new Conical shaped Niobium [18O] water Targets, # Belgian patent BE109556A3 / International application WO2012005970A1.

[13] M. Kostal, M. Schulc, V. Rypar, et al., Validation of zirconium isotopes (n, g) and (n, 2n) cross sections in a comprehensive LR-0 reactor operative parameters, Appl. Radiat. Isot. 128 (2017) 92–100.

[14] T. Goorley, et al., Initial MCNP6 release overview, Nucl. Technol. 180 (2012) 298–315.

[15] M. Veškrna, Z. Matěj, F. Mravec, V. Přenosil, F. Cvachovec, M. Košťál, Digitalized two parametric system for gamma/neutron spectrometry, in: 18th Topical Meeting of the Radiation Protection & Shielding Division of ANS, Knoxville, TN USA, 2014.

[16] Z. Matěj, Digitalization of Spectrometric System for Mixed Field of Radiation, LAP LAMBERT Academic Publishing, Saarbrücken, ISBN: 978-3-659-59970-5, 2014, p. 136 s.

[17] www.vfnuclear.com/en/neutron-gamma-analyser-nga-01.

[18] https://www.hamamatsu.com/resources/pdf/etd/PMT_handbook_v3aE.pdf.

[19] M. Košťál, Z. Matěj, E. Losa, O. Huml, M. Štefánik, F. Cvachovec, M. Schulc, B. Jánský, E. Novák, D. Harutyunyan, V. Rypar, On similarity of various reactor spectra and 235U Prompt Fission Neutron Spectrum, Appl. Radiat. Isot. 135 (2018) 83–91.

[20] J. Cvachovec, F. Cvachovec, Maximum likelihood estimation of a neutron spectrum and associated uncertainties, Adv. Mil. Technol. 1 (2) (2007) 5–28.

[21] E. Tomarchio, S. Rizzo, Coincidence-summing correction equations in gamma-ray spectrometry with p-type HPGe detectors, Radiat. Phys. Chem. 80 (2011) 318–323.

[22] L.R. Greenwood, C.D. Johnson, User Guide for the STAYSL PNNL Suite of Software Tools, PNNL-22253 Pacific North West National Laboratory, 2013.

[23] F.G. Perey, Least-Squares Dosimetry unfolding: The Program STAY'SL. ORNL/TM-6062, Oak Ridge National Laboratory.

[24] Standard Guide for an Application of Neutron Spectrum Adjustment Methods in reactor Surveillance, E 706 (IIA). ASTM E 944-08, ASTM International.

[25] M. Reginatto, Overview of spectral unfolding techniques and uncertainty estimation, Rad. Meas. 45 (10) (2010) 1323–1329.

[26] K.K. Gudima, S.G. Mashnik, Cascade-exciton model of nuclear reactions, Nuclear Phys. A 401 (2) (1983) 401-329.

[27] A.C. Kraan, Range verification methods in particle therapy underlying physics and Monte Carlo modeling, Front. Oncol. 5 (2015) http://dx.doi.org/10.3389/fonc.2015.00150.

[28] H.W. Bertini, Low energy intranuclear cascade calculations, Phys. Rev. 131 (4) (1963) 1801–1821.

[29] H.W. Bertini, Low energy intranuclear cascade calculations Phys. Rev. 138, AB2, erratum of : "Phys. Rev. Vol. 131(4), (1963), pp. 1801-1821".

[30] A.J. Koning, D. Rochman, Modern nuclear data evaluation with the TALYS code system, Nucl. Data Sheets 113 (2012) 2841–2934.

[31] R.A. Forrest, et al., Report INDC(NDS)-628, (2013).

[32] R. Capote, K.I. Zolotarev, V.G. Pronyaev, A. Trkov, J. ASTM Int. (JAI)- 9 (4) (2012) JAI104119.

[33] E.M. Zsolnay, R. Capote, H.K. Nolthenius, A. Trkov, Technical report INDC(NDS)-0616, IAEA, Vienna, 2012.

[34] P.J. Griffin, Covariance propagation in spectral indices, Nucl. Data Sheets 123 (2015) 104–108.

[35] Recommended cross sections for 18O(p, n)18F reaction https://www-nds.iaea.org/medical/o8p18f0.html.

[36] T. Amin, A. Infantino, R. Barlow, C. Hoehr, Validating production of PET radionuclides in solid and liquid targets, Comparing Geant4 predictions with FLUKA and measurements, Appl. Radiat. Isot. 133 (2018) 61–67.

[37] F. Cvachovec, Z. Bures, M. Komarek, et al., Support of Mathematical and Physical Research, Final Report of Specific Research in 2006, the University of Defence in Brno, pp. 2–6.